

Development of the normalization method for the Jagiellonian PET scanner

AURÉLIEN COUSSAT (1,2,*), WOJCIECH KRZEMIEN (3,2),
JAKUB BARAN (1,2), SZYMON PARZYCH (1,2)

- (1) Faculty of Physics, Astronomy and Applied Computer Science, Jagiellonian University, 30-348 Kraków, Poland,
(2) Centre for Theranostics, Jagiellonian University, 31-501 Kraków, Poland,
(3) High Energy Physics Division, National Centre for Nuclear Research, Otwock, Swierk, PL-05-400, Poland
(* *Corresponding author: Aurélien Coussat, aurelien.coussat@uj.edu.pl*)

FOR THE J-PET COLLABORATION

Received September 4, 2024

This work aims at applying the theory of the component-based normalization for the Jagiellonian PET scanner, currently under development at the Jagiellonian University. In any Positron Emission Tomography acquisition, efficiency along a line-of-response can vary due to several physical and geometrical effects, leading to severe artifacts in the reconstructed image. To mitigate these effects, a normalization coefficient is applied to each line-of-response, defined as the product of several components. Specificity of the Jagiellonian PET scanner geometry is taken into account. Results obtained from GATE simulations are compared with preliminary results obtained from experimental data.

Keywords— Positron Emission Tomography, Jagiellonian PET, Normalization

1. Introduction

The Jagiellonian PET (J-PET) scanner is a high acceptance multi-purpose Positron Emission Tomography (PET) detector optimized for the detection of photons from positron-electron annihilation, currently under development at the Jagiellonian University [1–4]. The current prototype, named the Modular J-PET [5], is composed of 24 individual modules arranged cylindrically. Each module is composed of 13 plastic scintillator strips with a size of $24 \times 6 \times 500 \text{ mm}^3$. The scintillators are readout on both sides by a matrix of Silicon PhotoMultipliers [1].

Several effects impact the efficiency of detector strips, such as geometric effects or variation in detector intrinsic efficiencies. To counterbalance the non-uniformity

in efficiency, normalization factors can be incorporated into the image reconstruction procedure. This contribution is a first step towards proper normalization of the Modular J-PET scanner. Section 2 describes the normalization factors and how they are computed, Section 3 shows preliminary results and Section 4 briefly concludes.

2. Materials and Methods

2.1. Normalization coefficients

The proper determination of the normalization coefficient for a given line of response (LOR) permits to compensate for the detector efficiency variation, and for the geometrical effects not included in the projection model. The lack of those corrections leads to artifacts generation and the degradation of the final image quality [6]. The so called component-based normalization method [7] relies on factorization of the normalization coefficients into sub-components that can be estimated separately, and on usage of the fan-sums strategy to lower the variance of the estimations. This work adapts the definitions of Pépin *et al.* [8].

Unlike conventional PET scanners, whose detectors are divided into several crystals, the J-PET scintillator strips are continuous in the axial direction. We nevertheless define M virtual bins in the axial direction. We also denote as L the number of strips (312 in the case of the Modular J-PET scanner). The LOR that joins portion u of strip i with portion v of strip j is denoted "LOR $uivj$ ". These definitions are illustrated in Fig. 1.

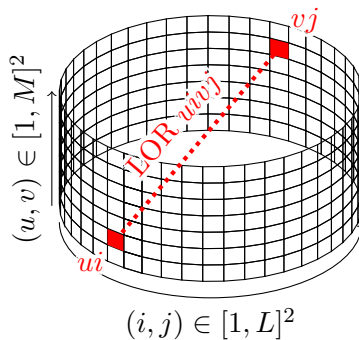


Fig. 1: LORs definition.

The normalization coefficient for a given LOR is given by the product of several normalization factors. Each of these factors accounts for a different effect. The normalization coefficient for the LOR $uivj$ is given as [8]

$$\eta_{uivj} = b_u^{\text{ax}} \cdot b_v^{\text{ax}} \cdot g_{uv}^{\text{ax}} \cdot g_{ij}^{\text{tr}} \cdot f_{ij}^{\text{tr}} \cdot \epsilon_{ui} \cdot \epsilon_{vj} \quad (1)$$

where b^{ax} represents the axial block profile factors, g^{ax} the axial geometric factors, g^{tr} the transverse geometric factors, f^{tr} the transverse interference function and ϵ the intrinsic detector efficiencies. Note that transverse interference functions are

designed to compensate for non-uniformity of detection efficiency with respect to the location of a crystal in a detector block, and can be ignored in the context of the J-PET scanner due to the design of its detectors.

Axial block profile factors, axial geometric factors, and intrinsic detector efficiencies are computed from the acquisition of a uniform cylindrical source centered on the scanner axis, and we denote as t_{uivj}^{cyl} the number of true coincidences measured along LOR $uivj$ during the acquisition. Transverse geometric factors are computed from the acquisition of a uniform annular source, and we denote as t_{uivj}^{ann} the number of true coincidences measured along LOR $uivj$ during the acquisition. ‘‘True coincidences’’ refer here to coincidences that have not undergone any scattering (in the phantom or in the detector) and that are not accidental.

Axial block profile factors b^{ax} normalize true coincidences along axial planes, that is the planes comprising the LOR whose detectors are located at the same axial position ($u = v$). They are defined as

$$b_u^{\text{ax}} = \sqrt{\frac{\frac{1}{M} \sum_{v=1}^M \sum_{i=1}^L \sum_{j=1}^L t_{vivj}^{\text{cyl}}}{\sum_{i=1}^L \sum_{j=1}^L t_{uiuj}^{\text{cyl}}}}. \quad (2)$$

Axial geometric factors account for efficiency variations caused by the detector geometry in the axial direction. They are defined between two axial positions u and v as

$$g_{uv}^{\text{ax}} = \frac{\frac{1}{M^2} \sum_{u'=1}^M \sum_{v'=1}^M b_{u'}^{\text{ax}} \cdot b_{v'}^{\text{ax}} \sum_{i=1}^L \sum_{j=1}^L t_{u'iv'j}^{\text{cyl}} \cos \theta}{b_u^{\text{ax}} \cdot b_v^{\text{ax}} \sum_{i=1}^L \sum_{j=1}^L t_{uivj}^{\text{cyl}} \cos \theta} \quad (3)$$

where θ is the angle between the LOR and the transverse plane.

Transverse geometric factors also account for efficiency variations caused by the detector geometry, but this time along transverse planes. They are defined for a radial distance $r \in [1; K]$, where K is the number of radial bins, as

$$g_r^{\text{tr}} = \frac{\frac{1}{K} \sum_{r'=1}^K \sum_{u=1}^M \sum_{v=1}^M \sum_{i=1}^L \sum_{j=1}^L c_{vivj}^{\text{ann}} \Big|_{x_r(i,j)=r'}}{\sum_{u=1}^M \sum_{v=1}^M \sum_{i=1}^L \sum_{j=1}^L c_{vivj}^{\text{ann}} \Big|_{x_r(i,j)=r}} \quad (4)$$

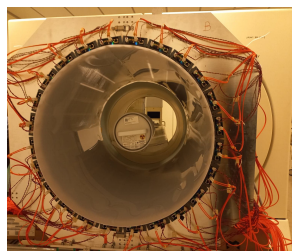
where $x_r(i, j)$ represents the radial distance for the LOR joining strips i and j , and where c_{vivj}^{ann} represents the number of coincidence for LOR $uivj$ with the correction given by $c_{vivj}^{\text{ann}} = a_{uivj} \cdot b_u^{\text{ax}} \cdot b_v^{\text{ax}} \cdot g_{uv}^{\text{ax}} \cdot \epsilon_{ui} \cdot \epsilon_{vj} \cdot t_{uivj}^{\text{ann}}$. Here, a_{uivj} corresponds to the inverse of the analytical projection of the source.

Intrinsic detector efficiency ϵ_{ui} represents the ability of the strip portion located at ring u and strip i to convert gamma photons into light. This parameter is computed using the fan-sum algorithm as

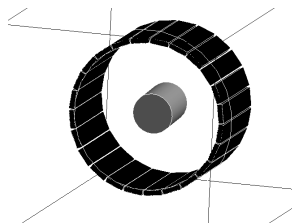
$$\epsilon_{ui} = \frac{\frac{1}{L} \sum_{i'=1}^L \sum_{v=1}^M \sum_{j=1}^L t_{ui'vj}^{\text{cyl}}}{\sum_{v=1}^M \sum_{j=1}^L t_{uivj}^{\text{cyl}}}. \quad (5)$$

2.2. Data acquisition

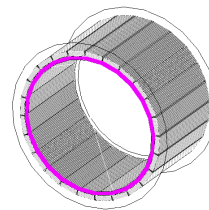
In order to compute the normalization factors, the acquisition of a Siemens CS-27 cylindrical phantom was performed. The cylinder was 50 cm long, had a radius of 10 cm, and a capacity of 8407 mL. The cylinder was filled with 88.43 MBq of Gallium-68 and placed at the center of the Modular J-PET. The setup is shown in Fig. 2a. Note that we have not performed any coincidence filtering in this case. At this stage of development, we consider the effect of scattered and accidental coincidences as negligible, and we leave their filtering for future works.



(a) Data acquisition from a cylindrical phantom.



(b) Monte Carlo simulation of a uniform cylindrical phantom.



(c) Monte Carlo simulation of a uniform annular phantom (in pink, not to scale).

Fig. 2: Data acquisition setups.

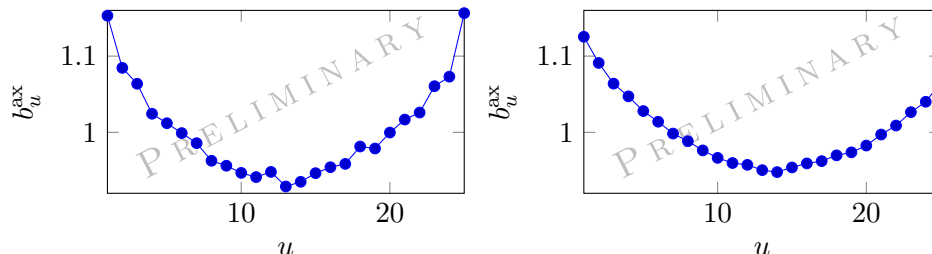
Two simulations of both a cylindrical and an annular phantom were also performed using the *GEANT4 Application for Tomographic Emission* (GATE) [9]. The cylindrical setup simulates a 1800 s acquisition of the cylinder described above, with an activity of 100 MBq, placed at the center of the detector. The cylindrical simulation setup is illustrated by Fig. 2b. The annular simulation was performed using a moving ring source. The ring source was 1 cm thick and 2.5 mm long with 10 MBq of activity. A number of 200 positions were axially simulated, each simulating 100 s of acquisition, resulting in a total time of 20 000 s. The annular simulation setup is illustrated by Fig. 2c. In both simulations, the scattered and accidental coincidences were completely filtered out based on recorded hit data, resulting in 5.08×10^7 true coincidences (out of 8.77×10^7 coincidences, 57.90 %) for the cylindrical phantom, and 8.96×10^7 true coincidences (out of 1.20×10^8 coincidences, 74.91 %) for the annular phantom.

Values used for the various parameters described in Section 2.1 are the following: $M = 25$, $L = 312$, $K = 25$.

3. Preliminary results

Figure 3 shows the axial geometric factors b^{ax} . The lower values near the axial center of the scanner denote a higher detection efficiency. The results from Monte Carlo data (Fig. 3a) display stronger fluctuations than those from real data (Fig. 3b) probably due to the lower statistics of the Monte Carlo sample. On the other hand, the factors obtained with real data are asymmetric: we suppose that

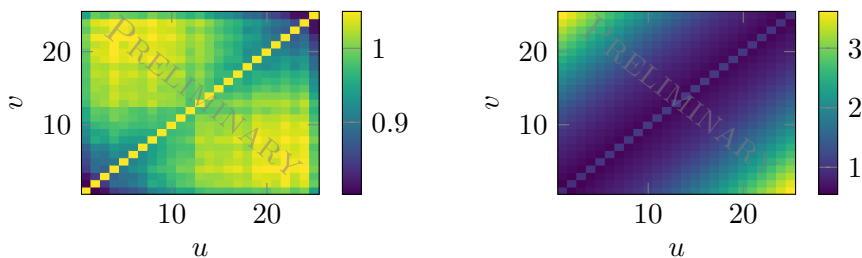
this is due to the cylinder being slightly tilted by about 3° during the acquisition. Further investigations are required to conclude on this observation.



(a) Computed from Monte Carlo data. (b) Computed from cylinder acquisition.

Fig. 3: Axial block profile factors (b_u^{ax}). Lines between data points illustrate the trend but do not refer to data interpolation.

Figure 4 shows the axial geometric factors g^{ax} . As expected from the definition of the axial geometric factors (Eq. (3)), the factors are constant along the diagonal, that is where $u = v$. At the edges, where the ring difference is large, the efficiency is lower due to the decreased probability of the LORs, hence the higher values of the axial geometric factors. Note the difference in color scale between Fig. 4a and Fig. 4b: we suggest that these are due to LOR obliqueness and the coincidence filtering strategy applied by the J-PET scanner with respect to ring difference. However, further investigations are needed to validate our hypothesis.

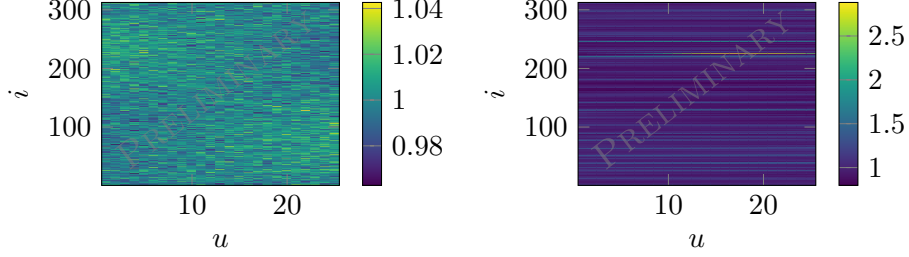


(a) Computed from Monte Carlo data. (b) Computed from cylinder acquisition.

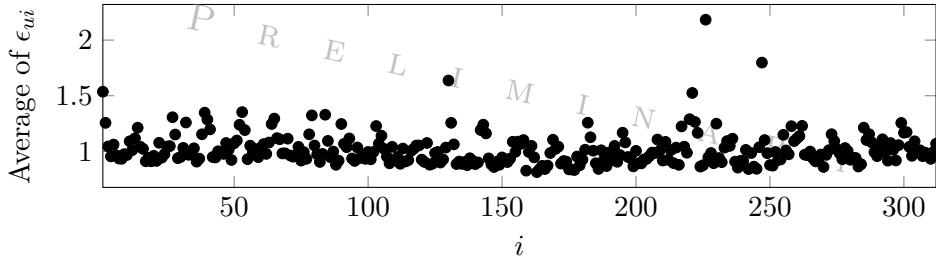
Fig. 4: Axial geometric factors (g^{ax}).

Figure 5 shows the intrinsic detector efficiencies ϵ . In Fig. 5a, as we considered a GATE simulation with perfect detectors and uniform efficiencies, the factors are uniform and the small variations that appear are entirely due to statistical noise. On the other hand, Fig. 5b highlights which areas of the detectors have a lower efficiency. Figure 5c averages on a strip-basis the values presented in Fig. 5b, which makes the anomalies clearly appear.

Figure 6 shows the transverse geometric factors g^{tr} . The low values for large radial distances show that efficiency is higher near the edge of the field of view, as expected from the geometry of the detector strips, due to the LOR obliqueness.



(a) Computed from Monte Carlo data. (b) Computed from cylinder acquisition.



(c) Average value of ϵ_{ui} for each strip i .

Fig. 5: Intrinsic detector efficiencies (ϵ).

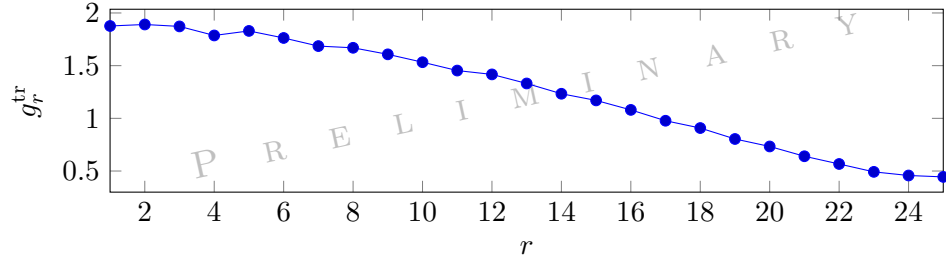


Fig. 6: Transverse geometric factors (g^{tr}). Lines between data points illustrate the trend but do not refer to data interpolation. This result is Monte Carlo-based only due to the lack of a dedicated measurement.

4. Discussion and conclusions

Normalization components highlight the relative importance of several physical and geometrical effects. They can be used to obtain insights of the efficiency of different aspects of the scanner, such as the efficiency of the detectors, or the scanner response with respect to LOR obliqueness. Due to the design of the J-PET scanner, where the detector strips are axially continuous, the definition of some normalization factors must be adapted. Future work consists of interpolating the normalization factors that have an axial dependency in order to compute normalization factors for any point along the whole strip, and to assess the improvements

in image quality when taking into account all the normalization factors during image reconstruction. The final goal is to apply the same procedure to the future Total-Body J-PET scanner [10, 11].

5. Acknowledgments

The authors acknowledge the support provided by the Foundation for Polish Science through the TEAM POIR.04.04.00-00-4204/17 program; the National Science Centre of Poland through grants MAESTRO no. 2021/42/A/ST2/00423 and OPUS no. 2019/35/B/ST2/03562; the Ministry of Education and Science through grant no. SPUB/SP/490528/2021; the SciMat and qLIFE Priority Research Areas budget under the program *Excellence Initiative - Research University* at the Jagiellonian University, and Jagiellonian University project no. CRP/0641.221.2020.

References

- [1] L. Raczyński *et al.*, “Novel method for hit-position reconstruction using voltage signals in plastic scintillators and its application to positron emission tomography,” *Nuclear Instruments and Methods in Physics Research Section A: Accelerators, Spectrometers, Detectors and Associated Equipment*, vol. 764, pp. 186–192, 2014.
- [2] P. Moskal *et al.*, “Positronium imaging with the novel multiphoton PET scanner,” *Science Advances*, vol. 7, no. 42, eabh4394, 2021.
- [3] P. Moskal *et al.*, “Testing CPT symmetry in ortho-positronium decays with positronium annihilation tomography,” *Nature Communications*, vol. 12, no. 1, pp. 1–9, 2021.
- [4] S. Niedźwiecki *et al.*, “J-PET: A new technology for the whole-body PET imaging,” *arXiv preprint arXiv:1710.11369*, 2017.
- [5] P. Moskal *et al.*, “Simulating NEMA characteristics of the modular total-body J-PET scanner—an economic total-body PET from plastic scintillators,” *Physics in Medicine & Biology*, vol. 66, no. 17, p. 175 015, Sep. 2021, ISSN: 0031-9155, 1361-6560. DOI: 10.1088/1361-6560/ac16bd.
- [6] D. L. Bailey, Ed., *Positron emission tomography: basic sciences*. New York: Springer, 2005, ISBN: 978-1-85233-798-8.
- [7] R. D. Badawi and P. K. Marsden, “Developments in component-based normalization for 3D PET,” *Physics in Medicine & Biology*, vol. 44, no. 2, pp. 571–594, Feb. 1999, ISSN: 0031-9155, 1361-6560. DOI: 10.1088/0031-9155/44/2/020.

- [8] A. Pépin, S. Stute, S. Jan, and C. Comtat, “Normalization of Monte Carlo PET data using GATE,” in *2011 IEEE Nuclear Science Symposium Conference Record*, Valencia, Spain: IEEE, Oct. 2011, pp. 4196–4200, ISBN: 978-1-4673-0120-6 978-1-4673-0118-3 978-1-4673-0119-0. DOI: 10.1109/NSSMIC.2011.6153804.
- [9] D. Sarrut *et al.*, “Advanced monte carlo simulations of emission tomography imaging systems with GATE,” *Physics in Medicine & Biology*, vol. 66, no. 10, 10TR03, 2021.
- [10] P. Moskal and E. Ł. Stepień, “Prospects and clinical perspectives of total-body PET imaging using plastic scintillators,” *PET Clinics*, vol. 15, pp. 439–452, 2020.
- [11] A. Alavi, T. J. Werner, E. Ł. Stepień, and P. Moskal, “Unparalleled and revolutionary impact of pet imaging on research and day to day practice of medicine,” *Bio-Algorithms and Med-Systems*, vol. 17, no. 4, pp. 203–212, 2021. DOI: doi:10.1515/bams-2021-0186.